High resolution seafloor thermometry and internal wave monitoring using Distributed Acoustic Sensing

Julián Peláez Quiñones[1], Anthony Sladen[2], Aurelien Ponte[3], Itzhak Lior[4], Jean-Paul Ampuero[2], Diane Rivet[2], Samuel Meulé[5], Frédéric Bouchette[5], Ivane Pairaud[3], and Paschal Coyle[6]

[1]Université Côte d'Azur, CNRS, Observatoire de la Côte d'Azur, IRD, Géoazur
[2]Université Côte d'Azur
[3]IFREMER
[4]Institute of Earth Sciences
[5]Geosciences-M/GLADYS
[6]Aix-Marseille Université

December 7, 2022

Abstract

Temperature is central for ocean science but is still poorly sampled on the deep ocean. Here, we show that Distributed Acoustic Sensing (DAS) technology can convert several kilometer long seafloor fiber-optic (FO) telecommunication cables into dense arrays of temperature anomaly sensors with milikelvin (mK) sensitivity, allowing us to monitor oceanic processes such as internal waves and upwelling with unprecedented detail. We validate our observations with oceanographic in-situ sensors and an alternative FO technology. Practical solutions and recent advances are outlined to obtain continuous absolute temperatures with DAS at the seafloor. Our observations grant key advantages to DAS over established temperature sensors, showing its transformative potential for thermometry in ocean sciences and hydrography.

High resolution seafloor thermometry and internal wave monitoring using Distributed Acoustic Sensing

Julián Pelaez Quiñones[1*], Anthony Sladen[1], Aurelien Ponte[2], Itzhak Lior[3], Jean-Paul Ampuero[1], Diane Rivet[1], Samuel Meulé[4], Frédéric Bouchette[4], Ivane Pairaud[2], Paschal Coyle[5]

[1]Université Côte d'Azur, CNRS, Observatoire de la Côte d'Azur, IRD, Géoazur, Sophia Antipolis, *250* rue Albert Einstein, *06560*, Valbonne, France
[2]IFREMER, Université de Brest, CNRS, IRD, Laboratoire d'Océanographie Physique et Spatiale, IUEM, Brest, France
[3]Institute of Earth Sciences, The Hebrew University, Jerusalem, Israel
[4]Geosciences-M/GLADYS, Université de Montpellier, CNRS, Montpellier, France
[5]Aix-Marseille Université, CNRS/IN2P3, CPPM, Marseille, France

Key Points:

- Low frequency DAS data on a seafloor fiber optic cable matches independent temperature observations
- DAS detects temperature variations down to less than 1 mK
- Ocean temperature variability of time scales of hours to days and spatial scales of hundreds of meters to several kilometers is captured

Corresponding author: *Julián Pelaez, `julian.pelaez@geoazur.unice.fr`

Abstract

Temperature is central for ocean science but is still poorly sampled on the deep ocean. Here, we show that Distributed Acoustic Sensing (DAS) technology can convert several kilometer long seafloor fiber-optic (FO) telecommunication cables into dense arrays of temperature anomaly sensors with milikelvin (mK) sensitivity, allowing us to monitor oceanic processes such as internal waves and upwelling with unprecedented detail. We validate our observations with oceanographic in-situ sensors and an alternative FO technology. Practical solutions and recent advances are outlined to obtain continuous absolute temperatures with DAS at the seafloor. Our observations grant key advantages to DAS over established temperature sensors, showing its transformative potential for thermometry in ocean sciences and hydrography.

Plain Language Summary

In recent years, technological advances enabled the transformation of standard fiber-optic cables into long arrays of sensors that finely detect physical changes of their surrounding environment along several kilometers at meter-scale samplings and less. One of these technologies, known as "Distributed Acoustic Sensing", is increasingly used to detect sound waves, mechanical vibrations and other external forces in diverse settings. Here we apply this technology on a several-kilometers-long telecommunication cable lying along the seafloor South of Toulon (France) to show that, over timescales of some hours and longer, the system is instead highly sensitive to small temperature fluctuations of the surrounding water. We show that these fluctuations are related to complex underwater processes that are widespread in the ocean and well-known to oceanographers but rarely measured continuously at such level of detail. The potential of this technology for oceanography and other marine sciences is thus highlighted.

1 Introduction

1.1 Relevance of ocean temperature variability and experimental challenges

Monitoring seafloor ocean temperature variability became a priority over the last years within the Oceanographic community (Johnson et al., 2015; Howe et al., 2019). On climatic timescales, bottom temperature measurements are needed to constrain the global ocean heat content and imbalance (Meyssignac et al., 2019), to monitor the evolution of water masses on regional scales (Margirier et al., 2020), climate changes (Wijffels et al., 2016) and to predict the chemical (Coogan & Gillis, 2018) and biological (Griffiths et al., 2017) evolution of the ocean. Improved seafloor measurements within the coastal domain are much needed given their poor representation in climatic models (Todd et al., 2019). Temperature variability at the timescale of hours to minutes affects: the degree of homogeneity of the water column and ocean circulation (Woodson, 2018), the vertical transport of nutrients for marine productivity (Villamaña et al., 2017) and the propagation of hydroacoustic waves (Wang et al., 2020). The bottom boundary layer dynamics also remains an area of forefront research in both the coastal domain (Burchard et al., 2008; Trowbridge & Lentz, 2018) and the abyss (Ruan et al., 2017; Naveira-Garabato et al., 2019).

Ocean in-situ thermometry typically relies on scattered point measurements and temporary deployments near the water surface (e.g. ships with thermosalinographs, buoys), which tend to be limited in terms of temporal and spatial resolution, while access to the deep ocean and remote regions remains challenging. Oceanographic moorings, Remotely Operated Vehicles, i.a. have attempted to fill this gap. However, obtaining large spatial coverage and long-term continuous measurements remains difficult (Favali & Beranzoli, 2006).

1.2 DAS Thermometry

In recent years, efforts have been devoted to transform fiber-optic (FO) cables into dense arrays of sensors with technologies that leverage various back-scattering effects of light (Hartog, 2000; Li et al., 2021). Among these, Distributed Acoustic Sensing (DAS) has gained wide interest thanks to its ability to monitor seismo-acoustic signals and dynamic strain with high sensitivity, making it suitable for a wide range of monitoring applications (e.g. Becker & Coleman, 2019; Lindsey et al., 2019; Sladen et al., 2019; Williams et al., 2019; Cheng et al., 2021; Matsumoto et al., 2021; Rivet et al., 2021; Ugalde et al., 2021; Bouffaut et al., 2022; Guerin et al., 2022; Williams et al., 2022).

Fluctuations in both the mechanical strain and temperature fields locally change the optical path length of the fiber which is sensed by DAS interrogators (López-Higuera, 2002; Hartog, 2017; Lu et al., 2017). At short timescales ($\lesssim$10 ms), DAS records mostly strain signals as ambient temperature usually fluctuates more slowly, while at longer timescales, the temperature effect is expected to dominate over strain, presumably due to changes in the fiber refractive index (Ide et al., 2021). Ide et al. (2021) analysed the low frequency (LF) component of DAS signals acquired on a cable offshore Japan. They suggested that these signals were related to the thermal signature of water currents and linked them to interaction between tides, complex bathymetry and currents. Lindsey et al. (2019) had also speculated about possible internal waves (IWs) signatures on LF-DAS data collected offshore California, USA. In practice however, the role of temperature in LF-DAS signals remains to be demonstrated.

Additionally to DAS, Distributed Fiber Optic Sensing (DFOS) can be performed with alternative technologies, such as: Distributed Temperature Sensing (DTS) and Distributed Strain and Temperature Sensing (DSTS). While DAS relies on Rayleigh scattering and measures variations in the phase of the back-scattered light, DTS and DSTS track variations in the Raman and Brillouin back-scattered light spectrum, respectively (Hartog, 2017). For instance, Connolly and Kirincich (2019); Reid et al. (2019) and Davis et al. (2020) implemented DTS to track near-coastal seafloor temperatures and observed IWs, cooling events and tidal currents.

In this study, we analyse LF-DAS ($\lesssim$1 mHz) signals on a seafloor telecommunication cable in the South of France. We compare our results with independent ocean temperature measurements and DSTS data. We show that the recorded anomalies are related to IWs and upwelling events, and mainly, if not fully, related to temperature effects.

2 Materials and Methods

2.1 Low-frequency DAS

Our analysis focuses on nearly two weeks of data of a DAS campaign operated on July 2019 on a seafloor cable extending almost 45 km from Toulon, France, towards the Mediterranean basin (Fig. 1). The data were acquired with a phase-sensitive Optical Time-Domain Reflectometry (ϕ-OTDR) chirped-pulse DAS acquisition system (Pastor-Graells et al., 2016; Fernández-Ruiz et al., 2019), providing strain measurements with a spatial sampling and gauge length of 10 m.

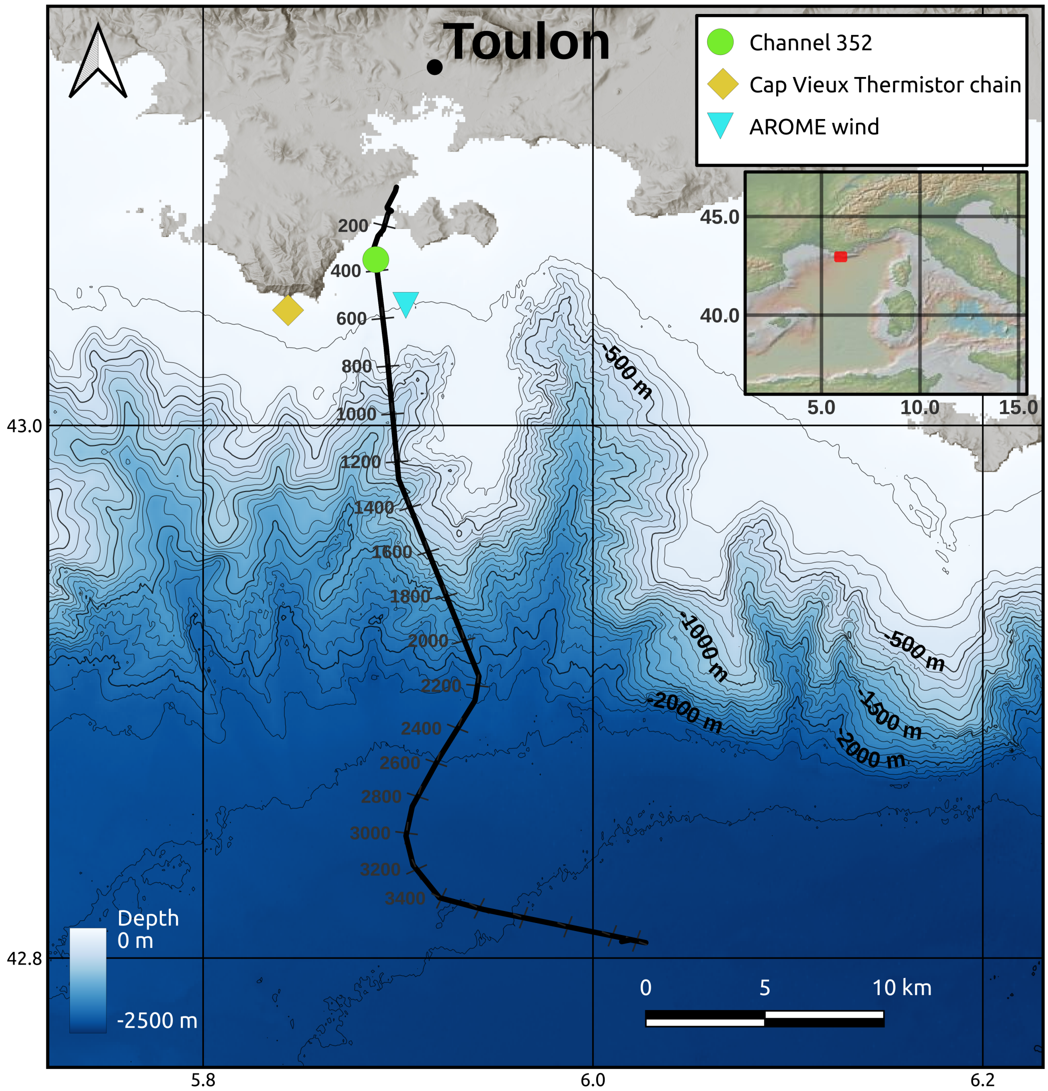

Figure 1. Toulon seafloor FO cable layout (black curve; numbered channels indicated) in the Mediterranean sea. Bathymetry obtained from SHOM (2015). In Sec. 3, the temperature data of the thermistor chain (yellow diamond) is compared to channel 352 (green dot) of the cable. Data of the AROME wind model are extracted at the position of the blue inverted triangle.

For a complete description of the acquisitions, see Supplementary Text S1 and Lior et al. (2021).

To isolate the LF content ($\lesssim$ 1mHz) of the large DAS dataset (11 Terabytes) and make it manageable for signal processing in a standard workstation, we applied a temporal moving average on the strain time series of each channel independently. Details on the pre-processing scheme are provided in Supplementary Text S2.

Then, to convert LF-DAS strain values into absolute temperature differences, we used the approximation (Ide et al., 2021): $\mathrm{d}\epsilon/\mathrm{d}T = n\alpha + \mathrm{d}n/\mathrm{d}T$, where where ϵ is the recorded strain, T the temperature, n the optical fiber refractive index and α its thermal expansion coefficient (see Supplementary Text S3 for details). Furthermore, LF-DAS and DSTS observations are expected to be mostly sensitive to temperature instead of fiber strain, given that the monitored fiber is loose inside the cable (Cherukupalli & Anders, 2020).

2.2 Oceanographic and meteorological data

Our interpretation of the LF-DAS measurements relies on the temperature reference provided by a vertical thermistor chain of 10 sensors (5 to 50 m depths) off Cap Vieux, Toulon (Fig. 1) recording every half-hour at ±0.2°C accuracy (Sartoretto et al., 2022). The deepest sensor is nearly on the seabed. These sensors are about 4 km west of the closest cable section, a distance comparable or shorter than the horizontal scales of the main processes observed in this study.

Additionally, hourly wind data (horizontal speed components at 10 m-height and turbulent surface stresses) of Météo-France operational forecasting atmospheric model AROME (Seity et al., 2011) near the cable is used to check for potential correlations between wind events and LF-DAS. The spatial sampling of this model is of 0.01° (∼1.3 km). Wind station data was not available near the cable.

3 Results

3.1 LF-DAS variability - Time series

3.1.1 Variability on multiple days timescales

Fig. 2 summarizes our LF-DAS observations. Only the first 25 km of cable (from the shoreline to the continental rise) are shown, given that the signal has lower SNR at longer ranges. The highest LF-DAS values represent the largest temperature variations relative to the baseline of each channel during the observation period. Equivalent temperature differences above 10 K are not plotted in Fig. 2a, as these are considered too large for typical ocean temperature variability and are presumably biased by coastal dynamics, potentially surface gravity wave-induced stresses. The evolution of apparent strain values of LF-DAS in the time-range space (Fig. 2a) indicates that the largest variability on multiple days timescales is found on the continental shelf (within 100 m water depths). This is consistent given the larger thermal stratification expected in the upper ocean in general.

The multiple-days temperature trend recorded at the Cap Vieux thermistor chain correlates well with the best-matching LF-DAS channel, 352 (Fig. 2d), which was constrained via maximum cross-correlation search (additional details in Supplementary Text S3). This channel is on the 40 m isobath, which is comparable to that of the Cap Vieux sensor at 50 m depth, also at the seafloor. A major cooling event towards the end of the DAS campaign coincides with an intense northwesterly

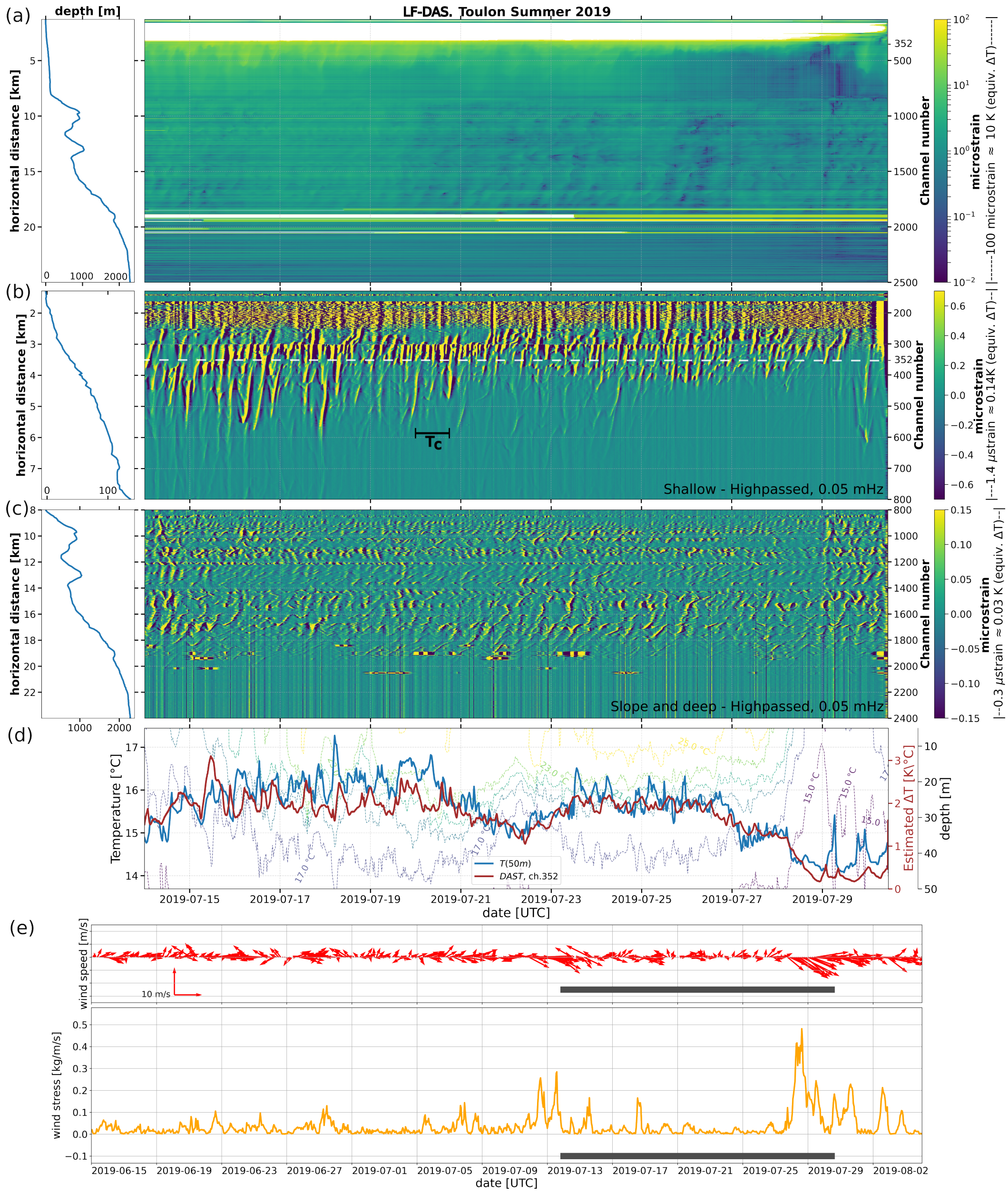

Figure 2. Toulon 2019 LF-DAS and ground truth time series. a) LF-DAS section from the shoreline to the deep Mediterranean sea with bathymetry along the cable (left). Anomalous data points corresponding approximately to $\Delta T > 10$ K were rejected. b) Highpass-filtered continental shelf and c) slope/rise subsections of (a) with adjusted colorscales. Channel 352 is marked in dashed line. For reference, the scale bar indicates the inertial period (T_c). d) Channel 352 LF-DAS time series approximated to absolute temperature differences (in red). The LF-DAS trace is offset vertically to align it with the mean value of the 50m-depth temperature time series on the thermistor chain (in blue). Isothermal contours extracted from the vertical thermistor chain are represented with dotted lines in colorscale (with depth scale in the far right) to depict the water column layering evolution. e) AROME horizontal wind vectors (above) and wind stress (below). The dark grey bars indicate the same time span of a) to d).

wind event lasting a few days as attested by the AROME data (Fig. 2e). No apparent dependency on wind events on the days before the deployment is visible.

3.1.2 Variability on multiple hours timescales

A marked variability in hourly-to-daily scales with distinctly non-sinusoidal waveforms (characteristic edginess, sharp onsets and decays) is evident in the LF-DAS sections (Figs. 2b-d). These shorter period oscillations are persistent from the shallow-most continental shelf down to almost the bottom of the continental slope at 2000 m depth. In the deep sea region, the fast common mode fluctuations reflect temperature variations close to or below the optical noise threshold of the DAS system. Some sporadic anomalous peaks on the deepest section of the slope are independently known to be related to hanging sections of the cable (Mata et al., submitted).

Hourly-to-daily fluctuations of LF-DAS on channel 352 exhibit some similarity with those of the Cap Vieux temperature, both in shape and periodicity (Fig. 2d). However, both time series are only roughly correlated at these timescales, which may be explained by the fact that the spatial scales associated with these fluctuations is smaller than the cable-thermistor chain separation. In general, the intermittent LF-DAS temperature arrivals (anomalies with slanted time-space offsets) in the shallow continental shelf (Fig. 2b) and deeper slope (Fig. 2c) indicate locally coherent propagation. Along the slope, a visible along-channel modulation of the LF-DAS patterns (amplitude and phase propagation) indicates a marked site control, potentially correlated with the bathymetry and also influenced by variable cable-seabed coupling and/or local variations in the fiber structure.

3.2 LF-DAS variability - Spectra

Fig. 3a shows Direct Fourier Transform periodograms using Welch's method for selected channel ranges, averaged on the shallow (channels 350-800), slope (800-2000) and deep (2000-3000) cable sections. The spectral peaks approach the mean inertial period in the study region, T_c=f_c^{-1}≈17.5h (f_c being the latitude-dependent Coriolis frequency) and its first harmonic, particularly at the shallow and slope sections (further details on inertial variability in Supplementary text S4). The deep section spectrum has a the weakest signal. As expected, these peaks are not correlated with the main tidal components, since the Mediterranean is a microtidal sea.

The short time span of the data hampers a FT-derived spectrogram that properly resolves LF signals in time. Furthermore, the markedly non-sinusoidal patterns of the LF-DAS time series affect the reliability of the finite Fourier Transform. In order to overcome these obstacles, we conduct an Empirical Mode Decomposition (EMD) analysis (Huang et al., 1998; Deering & Kaiser, 2005; Huang et al., 2009; Stallone et al., 2020; Quinn et al., 2021) based on the Hilbert-Huang transform (HHT) (Huang & Wu, 2008), which is intended for decomposion of non-linear and non-stationary signals. Supplementary text S5 describes details on the parameterization of the EMD and HHT.

Figs. 3b,c show the results of averaging the instantaneous frequencies of each of the EMD Intrinsic Mode Functions (IMFs, see Supplementary Text S5 and Fig. S1) obtained for each channel across the shelf and slope cable sections, respectively. The short-term variability correlates well with T_c in the study region, particularly in the slope section, where modulated inertial peak energy dominates (Fig. 3c). The spectral energy distribution in the shelf area (Fig. 3b) is comparatively more random and non-stationary, as expected from the time series signatures.

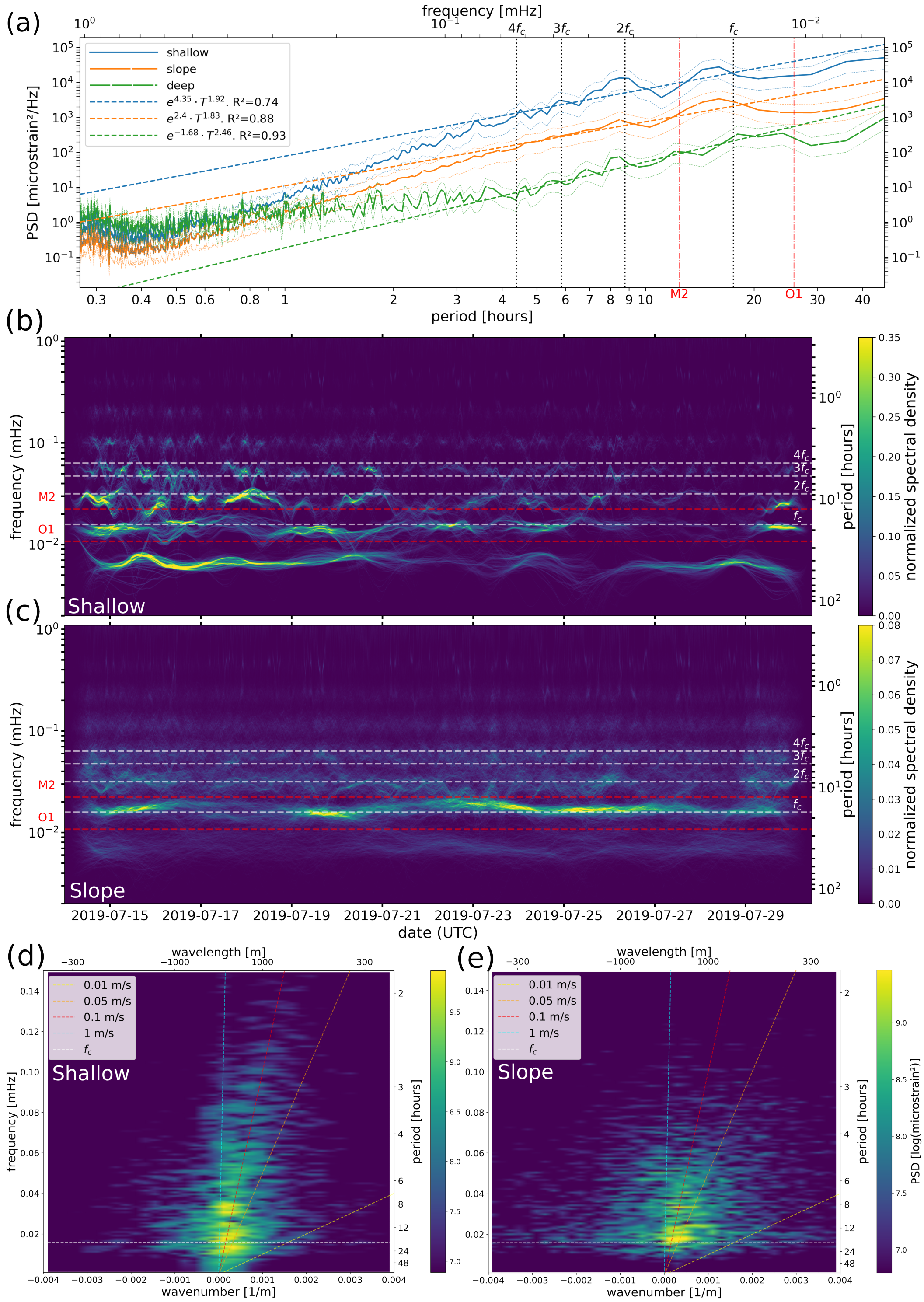

Figure 3. Toulon 2019 LF-DAS spectra (same time span as in Fig. 2). (a) Channel-averaged Welch spectra (6-day-long windows, 4-day overlaps) for different cable sections with 90% confidence intervals (Zhu et al., 2015). Linear regressions of the log-log spectra between 4 and 30 h are shown for reference, along with the inertial frequency f_c, its first three harmonics and the O_1 and M_2 tidal components. Average Hilbert-Huang spectra with tapered edges for the shallow (b) and slope (c) cable sections, and frequency-wavenumber spectra of the shallow (d) and slope (e) cable sections.

Several-days fluctuations as well as sporadic transient events are present in the shelf region, in contrast to the slope section, where steadier conditions are evident.

The marked presence of the inertial peak in the signals suggests near-inertial IWs. Figs 3d,e depict frequency-wavenumber (e.g. Margrave & Lamoureux, 2019) spectra on Continental shelf and slope sections where the horizontal cable projection is nearly linear. The apparent phase propagation speeds range from 0.01 to about 1 m/s. These are in good agreement with the typical phase propagation speeds of IWs in the ocean (e.g. Tintoré et al., 1995; Miropol'sky & Shishkina, 2013; Serebryany et al., 2020). Furthermore, a dominant shoreward propagation component (positive wavenumbers) is evident. The apparent wavelengths of the dominant processes range from a couple hundred of meters to several kilometers, also in line with typical wavelengths of IWs (Massel, 2015). The cable layout in the slope is affected by irregular bathymetry, which might partially explain the more smeared frequency-wavenumber spectrum on the latter (Fig. 3e). These plots further confirm the existence of near-inertial perturbations propagating above the cable. Furthermore, the repetitive and well-defined spectral energy bands along both, the shelf and slope, suggest higher-order modes of IWs.

4 Discussion and perspectives

4.1 Interpretation

4.1.1 Upwelling event

A cooling event corresponding to an estimated decrease of ~2 K across the continental shelf (~8 km-wide) is evidenced towards the end of the LF-DAS observation period (Figs. 2a-e) which is consistent with upwelling (Abrahams et al., 2021) caused by northwesterly mistral wind episodes in the region (Guenard et al., 2005; Odic et al., 2022). The independent Cap Vieux temperature measurements confirmed this cooling event which favored the homogenization of the water column temperature, and is consistent with decreased IWs during the last days analysed. Ocean currents, such as the near-surface Liguro-Provençal (i.e. Northern) current (Petrenko, 2003) could potentially be related to our observations, as these could produce temperature variations on multiple days timescales in the continental shelf and slope.

Ide et al. (2021) correlated deep offshore Japan LF-DAS data with temperature anomalies of a few Kelvins. Our LF-DAS observations also confirm temperature anomalies of some Kelvin on the continental shelf, and others on the order of ~0.1K on the continental slope seafloor off Toulon. Having in mind that standard FO and DAS systems have sensitivities of the order of a nanostrain, LF-DAS measurements should be sensitive to temperature variations of at least ~0.1 mK.

4.1.2 Near-inertial internal waves and higher frequency temperature variability

The LF-DAS observations reported here highlight the presence of near-inertial IWs producing temperature fluctuations of up to ~1 K at the seafloor from the coast and down to the continental rise. Weaker temperature variability of higher frequency is also present. The near-inertial variability is particularly ubiquitous over the continental slope which may be explained by the more stable thermal stratification there. Oscillations with periods of less than a couple hours are less obvious to interpret but are potentially related to the buoyancy frequency in the ocean, which is a well-known upper frequency bound for IWs. However, this spectral band might also be partially affected by optical noise. Complex reverberations on the rugged seafloor and deep-sea valleys of the slope might cause the harmonic-like spectral bands. Previous studies have also documented energetic near-coastal inertial IWs in the of Gulf of Lions (Millot & Crépon, 1981; Millot, 1990) and the Western Mediterranean abyss (Van Haren & the ANTARES collaboration, 2014).

Over the slope, LF-DAS points towards fluctuation amplitudes on the order of 0.01 K. Assuming a vertical thermal stratification of 10^{-3} K/m, such amplitudes amount to vertical displacements of about 10 m and near-inertial vertical velocity amplitudes of 10^{-3} m/s. On the seafloor, horizontal and vertical velocities are tied via bottom boundary condition: $w + \mathbf{u} \cdot \nabla h$ where w and $\mathbf{u}$ are the vertical and horizontal flows respectively, and h is water depth. Assuming an average slope of 0.1 (Fig. 2c), this leads to horizontal velocities of 0.01 m/s. These estimates of the horizontal and vertical flows are in line with past observations of IWs in the area (Van Haren & the ANTARES collaboration, 2014).

Our results show IWs with phase propagation having a dominant shoreward component (Fig. 3d,e). Remaining seaward energy could be partially comprised of horizontal reflections at bathymetric obstacles, as near-inertial IWs mostly reflect horizontally against slopping bottoms (Gerkema & Zimmerman, 2008). However, it is well-known that IW packets do not generally propagate horizontally. In fact, deep inertial motion has an upward phase component and downward group propagation when stratification (N) is larger than f_c (Tintoré et al., 1995). Both propagation vectors have equal-sign vertical components for gyroscopic IWs, that is when $N \approx 0$ (van Haren & Millot, 2004). Currently, LF-DAS on a single cable only provides a one-dimensional view of the multi-dimensional oceanic variability, therefore more advanced processing methods and additional constraints (e.g. multiple cables or additional ground truths) could provide further insights into IW propagation complexity.

The apparent propagation speeds of the temperature anomalies ($\sim$0.5 m/s) observed by Ide et al. (2021) are in line with the apparent propagation of IWs found in our study. The variable cross-shore range extent of temperature patterns over the shelf can be interpreted as variations in the amplitude of IW packets displacing the thermocline vertically at variable depths. Temporal variations in the temperature stratification could also be indirectly responsible for such differential patterns.

4.2 LF-DAS and alternative DFOS approaches

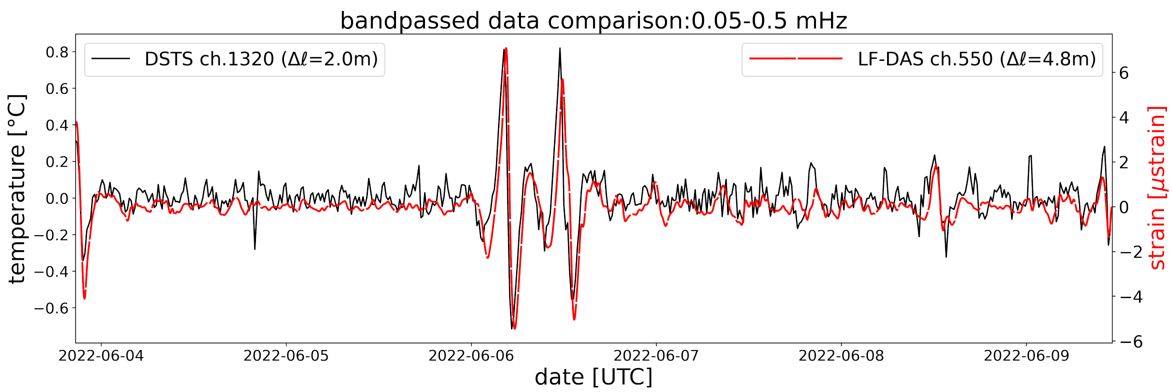

Figure 4. Comparison of DSTS and LF-DAS measurements at collocated channels in Toulon, June 2022, both bandpassed in the 0.05-0.5 mHz range.

Standard DAS and DSTS systems cannot distinguish temperature or strain anomalies without external information on the processes involved (e.g. frequency or shape of the perturbation). However, at LF the temperature effect is expected to dominate, as evidenced by the ground truth comparison in Sec. 3.

Upon calibration, DSTS and DTS are capable of providing absolute temperature measurements (e.g. Sinnett et al., 2020), while LF-DAS is currently limited to temperature variations estimates. Yet, LF-DAS has some key advantages when monitoring thermal anomalies: over short distances (∼5 km), most DSTS and DTS interrogators typically have repeatability (Hartog, 2017) on the order of 0.1∼1.0 K (also depending on type of fiber, duration of acquisition, environmental setting, i.a.), while LF-DAS approaches the ∼0.1 mK. For DSTS and DTS, the repeatability drops sharply with sensing range, e.g. ∼1.5 K at 70 km for a single-mode fiber with a minimum laser attenuation of 0.2 dB/km (Lauber et al., 2018). In contrast, the Rayleigh scattered power is 20 to 30 dB higher than the Brillouin and Raman scatterings typically used for temperature sensing, respectively (Santos & Farahi, 2014), so that longer sensing ranges are attainable with DAS (up to 80 km and more). At the same time, diverse techniques exist to preserve an optimal DAS repeatability at long distances (e.g. Shang et al., 2022).

To support our LF-DAS analysis, we ran an independent, simultaneous DAS and DSTS acquisition on the Toulon cable. Fig. 4 shows the LF-DAS and DSTS time series, bandpass-filtered from 0.05 to 0.5 mHz, a range where the frequency content of both instruments is comparable. Apart from some deviations in the weaker, fast fluctuations, LF-DAS matches the DSTS signal. The former appears smoother, potentially because of its longer spatial sampling (4.8 m for LF-DAS and 2.0 m for DSTS) and/or increased high frequency noise in the later. Apparent time lags are likely related to the different spatial samplings of each deployment and the absence of clock synchronization. Visual inspection of Supplementary Fig. S2 confirms the similarity of both data types and that the DSTS signal has a lower SNR at long ranges. Conversely, DSTS appears to have a higher SNR than LF-DAS near the shoreline, possibly due to increased sensitivity of DAS to surface gravity waves strain.

4.3 Challenges and limitations

Presently only absolute temperature anomalies can be estimated from LF-DAS because of the ϕ-OTDR limitations (Lu et al., 2017). The current lack of knowledge about the exact transfer function between the FO response and temperature, which could depend on cable material and structure (Ekechukwu & Sharma, 2021), hampers the retrieval of absolute temperatures. This, however, could be overcome by means of unique, temporary or regular temperature calibrations at a single or multiple cable locations with dedicated temperature sensors and/or with auxiliary DTS/DSTS systems, depending on the required precision and possible logistics. When implemented, the SMART cable initiative (Howe et al., 2022) should provide a calibrated temperature sensor at the optical repeaters of new cables. DAS is also making rapid progress in terms of performance. In a recent study, Vidal-Moreno et al. (2022) demonstrated the possibility to suppress the noise of DAS systems which increases inversely proportional to frequency, and thus opens the way for a new generation of DAS systems capable of providing absolute temperatures over periods of months or longer.

4.4 Perspectives: Opportunities for Oceanography from physics to biology

Our results highlight the potential of LF-DAS for high resolution thermometry in the underwater environment and for IW monitoring. In recent years, seismological and acoustical instrumentation has been used to study ocean phenomena (e.g. Grob et al., 2011; Traer et al., 2012; Davy et al., 2014; Ferretti et al., 2018; Wu et al., 2020; Song et al., 2021; Iafolla et al., 2022). DAS can likewise be implemented for these applications as well as to densely sample temperature signals, performing optimally in complex environments like the deep ocean. This provides new experimental opportunities for oceanographic and hydrographic applications such as long-term temperature monitoring of large water masses without the need for offshore campaigns, and could potentially be useful to study water circulation, turbulence, and to track geothermal heat transfer across the seafloor.

Acronyms

DAS Distributed Acoustic Sensing
DFOS Distributed Fiber Optic Sensing
DSTS Distributed Strain and Temperature Sensing
DTS Distributed Temperature Sensing
EMD Empirical Mode Decomposition
HHT Hilbert-Huang Transform
IW(s) Internal Wave(s)
LF-DAS Low-Frequency DAS
SNR Signal-to-Noise ratio
ϕ-OTDR Phase-sensitive Optical Time-Domain Reflectometry

5 Open Research

The fiber optic DSTS and the processed LF-DAS data, as well as times series used to produce Figs. 2-4, and S1-S2 are available in the following OSF repository: `https://osf.io/6jf9r` (`https://doi.org/10.17605/OSF.IO/6JF9R`). The main DAS dataset (Figs. 2,3 and S1) was recorded on the seafloor Toulon cable pertaining to the MEUST (Mediterranean Eurocentre for Underwater Sciences and Technologies) infrastructure (see Sladen et al. (2019) for details) using an Aragón Photonics hDAS interrogator. MEUST is financed with the support of the CNRSIN2P3, the Region Sud, France (CPER the State (DRRT), and FEDER. Auxiliary DAS and DSTS datasets were recorded on the same cable using a Febus Optics G1-C and a Febus A1-R interrogators, respectively. The latter were used to produce Figs. 4 and S2.

Bathymetry data of the study region (South of France/Gulf of Lions) to produce Fig. 1 was freely available at SHOM (2015) and can be accessed here: `https://diffusion.shom.fr/pro/mnt-facade-gdl-ca-homonim.html`. The map was produced with QGIS v3.22 (QGIS.org, 2022. QGIS Geographic Information System. QGIS Association).

The data of the thermistor chain of Cap Vieux is provided for free by Sartoretto et al. (2022) (`https://doi.org/10.17882/86522`) and can be retrieved upon request (Parameters: `Toulon_(CapSicie)`, 2019, All Depths) from the regional temperature observation network (T-MEDNet), `https://t-mednet.org/request-data?view=tdatarequest&site_id=38`. AROME operational atmospheric model data was obtained from Météo-France (`https://donneespubliques.meteofrance.fr/?fond=produit&id_produit=131&id_rubrique=51`).

Data processing and analyses largely relied on standard Python libraries, e.g. SciPy (`https://scipy.org/`), NumPy (`https://numpy.org/`), Pandas (`https://pandas.pydata.org/`), Matplotlib (`https://matplotlib.org/`), h5Py (`https://www.h5py.org/`); plus dedicated libraries for optimization: Dask (Dask Development Team, 2016); seismic data processing: ObsPy (Beyreuther et al., 2010); and additional specialized libraries: Sklearn (Pedregosa et al., 2011) and EMD (Quinn et al., 2021).

Acknowledgments

This work and J.P. were supported by the SEAFOOD project, funded by grant ANR-17-CE04-0007 of the French Agence Nationale de la Recherche, Université Côte d'Azur IDEX program UCA^{JEDI} ANR-15-IDEX-0001, and the Doeblin Federation (FR2800 CNRS). The June 2022 DAS acquisition was made possible by the MoniDAS project, funded by grant ANR-19-CE04-0011, of the French Agence Nationale de la Recherche, and the support of Febus Optics. The T-MEDNet project is funded by MPA-ENGAGE (Interreg Mediterranean Programme). We also want to thank Anne Molcard from the Mediterranean Institute of Oceanography (MIO), as well as Camille Jestin and Gaëtan Calbris from Febus Optics, for enriching suggestions and discussion.

References

Abrahams, A., Schlegel, R. W., & Smit, A. J. (2021). A novel approach to quantify metrics of upwelling intensity, frequency, and duration. *PLOS ONE*, *16*(7), 1-19. doi: 10.1371/journal.pone.0254026

Becker, M. W., & Coleman, T. I. (2019). Distributed Acoustic Sensing of Strain at Earth Tide Frequencies. *Sensors*, *19*(9). doi: 10.3390/s19091975

Beyreuther, M., Barsch, R., Krischer, L., Megies, T., Behr, Y., & Wassermann, J. (2010). Obspy: A python toolbox for seismology. *Seismological Research Letters*, *81*, 530-533. doi: 10.1785/gssrl.81.3.530

Bouffaut, L., Taweesintananon, K., Kriesell, H. J., Rørstadbotnen, R. A., Potter, J. R., Landrø, M., … et al. (2022). Eavesdropping at the speed of light: Distributed acoustic sensing of baleen whales in the arctic. *Frontiers in Marine Science*, *9*. doi: 10.3389/fmars.2022.901348

Burchard, H., Craig, P. D., Gemmrich, J. R., van Haren, H., Mathieu, P.-P., Meier, H. M., … et al. (2008). Observational and numerical modeling methods for quantifying coastal ocean turbulence and mixing. *Progress in Oceanography*, *76*(4), 399-442. doi: https://doi.org/10.1016/j.pocean.2007.09.005

Cheng, F., Chi, B., Lindsey, N., Dawe, T., & Ajo-Franklin, J. (2021). Utilizing distributed acoustic sensing and ocean bottom fiber optic cables for submarine structural characterization. *Scientific Reports*, *11*. doi: 10.1038/s41598-021-84845-y

Cherukupalli, S., & Anders, G. J. (2020). Distributed fiber optic sensing and dynamic rating of power cables. In (chap. 11). Wiley-IEEE Press.

Connolly, T. P., & Kirincich, A. R. (2019). High-resolution observations of subsurface fronts and alongshore bottom temperature variability over the inner shelf. *Journal of Geophysical Research: Oceans*, *124*(1), 593-614. doi: 10.1029/2018JC014454

Coogan, L. A., & Gillis, K. M. (2018). Low-Temperature Alteration of the Seafloor: Impacts on Ocean Chemistry. *Annual Review of Earth and Planetary Sciences*, *46*(1), 21-45. doi: 10.1146/annurev-earth-082517-010027

Dask Development Team. (2016). Dask: Library for dynamic task scheduling [Computer software manual]. Retrieved from `https://dask.org`

Davis, K. A., Arthur, R. S., Reid, E. C., Rogers, J. S., Fringer, O. B., DeCarlo,

T. M., & Cohen, A. L. (2020). Fate of internal waves on a shallow shelf. *Journal of Geophysical Research: Oceans*, *125*(5), e2019JC015377. doi: 10.1029/2019JC015377

Davy, C., Barruol, G., Fontaine, F., Sigloch, K., & Stutzmann, E. (2014). Tracking major storms from microseismic and hydroacoustic observations on the seafloor. *Geophys. Res. Letters*, *41*, 8825-8831. doi: 10.1002/2014GL062319

Deering, R., & Kaiser, J. (2005). The use of a masking signal to improve empirical mode decomposition. In *Proceedings. (icassp '05). ieee international conference on acoustics, speech, and signal processing, 2005.* (Vol. 4, p. iv/485-iv/488 Vol. 4). doi: 10.1109/ICASSP.2005.1416051

Ekechukwu, G., & Sharma, J. (2021). Well-scale demonstration of distributed pressure sensing using fiber-optic DAS and DTS. *Scientific Reports*, *11*, 12505. doi: 10.1038/s41598-021-91916-7

Favali, P., & Beranzoli, L. (2006). Seafloor observatory science: a review. *Annals of Geophysics*, *49*(2-3). doi: 10.4401/ag-3125

Fernández-Ruiz, M. R., Costa, L., & Martins, H. F. (2019). Distributed acoustic sensing using chirped-pulse phase-sensitive otdr technology. *Sensors*, *19*(20), 4368. doi: 10.3390/s19204368

Ferretti, G., Barani, S., Scafidi, D., Capello, M., Cutroneo, L., Vagge, G., & Besio, G. (2018). Near real-time monitoring of significant sea wave height through microseism recordings: An application in the Ligurian Sea (Italy). *Ocean and Coastal Management*, *165*, 185-194.

Gerkema, T., & Zimmerman, J. (2008). An introduction to internal waves. *Lecture notes, Royal NIOZ, Texel, 2008*.

Griffiths, H., Meijers, A., & Bracegirdle, T. (2017, 09). More losers than winners in a century of future Southern Ocean seafloor warming. *Nature Climate Change*, *7*, 749–754. doi: 10.1038/NCLIMATE3377

Grob, M., Maggi, A., & Stutzmann, E. (2011). Observations of the seasonality of the antarctic microseismic signal, and its association to sea ice variability. *Geophysical Research Letters*, *38*(11). doi: 10.1029/2011GL047525

Guenard, V., Drobinski, P., Caccia, J.-L., Campistron, B., & Bench, B. (2005). An observational study of the mesoscale mistral dynamics. *Boundary-Layer Meteorology*, *115*, 263-288. doi: 10.1007/s10546-004-3406-z

Guerin, G., Rivet, D., van den Ende, M., Stutzmann, E., Sladen, A., & Ampuero, J. P. (2022). Quantifying microseismic noise generation from coastal reflection of gravity waves recorded by seafloor DAS. *Geophysical Journal International*, *231*. doi: 10.1093/gji/ggac200

Hartog, A. (2000). Distributed fiber-optic sensors: principles and applications. In *Optical fiber sensor technology* (pp. 241–301). Springer.

Hartog, A. (2017). *An Introduction to Distributed Optical Fibre Sensors* (1st ed.). CRC Press. doi: 10.1201/9781315119014

Howe, B. M., Angove, M., Aucan, J., Barnes, C. R., Barros, J. S., Bayliff, N., ... et al. (2022). SMART Subsea Cables for Observing the Earth and Ocean, Mitigating Environmental Hazards, and Supporting the Blue Economy. *Frontiers in Earth Science*, *9*. doi: 10.3389/feart.2021.775544

Howe, B. M., Arbic, B. K., Aucan, J., Barnes, C. R., Bayliff, N., Becker, N., ... et al. (2019). SMART Cables for Observing the Global Ocean: Science and Implementation. *Frontiers in Marine Science*, *6*. doi: 10.3389/fmars.2019.00424

Huang, N. E., Shen, Z., Long, S. R., Wu, M. C., Shih, H. H., Zheng, Q., ... et al. (1998). The empirical mode decomposition and the Hilbert spectrum for nonlinear and non-stationary time series analysis. *Proc. R. Soc. Lond. A.*, *454*, 903–995. doi: 10.1038/s41598-020-72193-2

Huang, N. E., & Wu, Z. (2008). A review on Hilbert-Huang transform: Method and its applications to geophysical studies. *Reviews of Geophysics*, *46*(2). doi: 10

Draft

.1029/2007RG000228
Huang, N. E., Wu, Z., Long, S. R., Arnold, K. C., Chen, X., & Blank, K. (2009). On instantaneous frequency. *Advances in Adaptive Data Analysis*, *01*(02), 177-229. doi: 10.1142/S1793536909000096

Iafolla, L., Fiorenza, E., Chiappini, M., Carmisciano, C., & Iafolla, V. A. (2022). Sea wave data reconstruction using micro-seismic measurements and machine learning methods. *Frontiers in Marine Science*, *9*. doi: 10.3389/fmars.2022.798167

Ide, S., Araki, E., & Matsumoto, H. (2021). Very broadband strain-rate measurements along a submarine fiber-optic cable off cape muroto, nankai subduction zone, japan. *Earth Planets Space*, *73*(63). doi: 10.1186/s40623-021-01385-5

Johnson, G. C., Lyman, J. M., & Purkey, S. G. (2015). Informing Deep Argo Array Design Using Argo and Full-Depth Hydrographic Section Data. *Journal of Atmospheric and Oceanic Technology*, *32*(11), 2187 - 2198. doi: 10.1175/JTECH-D-15-0139.1

Lauber, T., Cedilnik, G., & Lees, G. (2018). Physical Limits of Raman Distributed Temperature Sensing - Are We There Yet? In *26th international conference on optical fiber sensors* (p. WF30). doi: 10.1364/OFS.2018.WF30

Li, Y., Karrenbach, M., & Ajo-Franklin, J. B. (2021). A Literature Review: Distributed Acoustic Sensing (DAS) Geophysical Applications Over the Past 20 Years. *Distributed Acoustic Sensing in Geophysics: Methods and Applications*, 229–291. doi: 10.1002/9781119521808.ch17

Lindsey, N. J., Dawe, T. C., & Ajo-Franklin, J. B. (2019). Illuminating seafloor faults and ocean dynamics with dark fiber distributed acoustic sensing. *Science*, *366*(6469), 1103-1107. doi: 10.1126/science.aay5881

Lior, I., Sladen, A., Rivet, D., Ampuero, J.-P., Hello, Y., Becerril, C., ... et al. (2021). On the detection capabilities of underwater Distributed Acoustic Sensing. *Journal of Geophysical Research: Solid Earth*, *126*(3), e2020JB020925. doi: 10.1029/2020JB020925

Lu, X., Soto, M. A., & Thévenaz, L. (2017). Temperature-strain discrimination in distributed optical fiber sensing using phase-sensitive optical time-domain reflectometry. *Opt. Express*, *25*(14), 16059-16071. doi: 10.1364/OE.25.016059

López-Higuera, J. M. (Ed.). (2002). *Handbook of Optical Fibre Sensing Technology* (1st ed.). John Wiley & Sons, ltd.

Margirier, F., Testor, P., Heslop, E., Mallil, K., Bosse, A., Houpert, L., ... et al. (2020, 12). Abrupt warming and salinification of intermediate waters interplays with decline of deep convection in the Northwestern Mediterranean Sea. *Scientific Reports*, *10*. doi: 10.1038/s41598-020-77859-5

Margrave, G. F., & Lamoureux, M. P. (2019). *Numerical Methods of Exploration Seismology: With Algorithms in MATLAB®*. Cambridge University Press.

Massel, S. (2015). *Internal gravity waves in the shallow seas* (1st ed.). Springer Cham.

Mata, D., Ampuero, J.-P., Mercerat, D., Rivet, D., & Sladen, A. (submitted). Monitoring Deep Sea Currents with Seafloor Distributed Acoustic Sensing. *manuscript submitted to Journal of Geophysical Research: Oceans*.

Matsumoto, H., Araki, E., Kimura, T., Fujie, G., Shiraishi, K., Tonegawa, T., ... Karrenbach, M. (2021). Detection of hydroacoustic signals on a fiber-optic submarine cable. *Scientific Reports*, *11*. doi: 10.1038/s41598-021-82093-8

Meyssignac, B., Boyer, T., Zhao, Z., Hakuba, M. Z., Landerer, F. W., Stammer, D., ... et al. (2019). Measuring global ocean heat content to estimate the earth energy imbalance. *Frontiers in Marine Science*, *6*. doi: 10.3389/fmars.2019.00432

Millot, C. (1990). The Gulf of Lions' hydrodynamics. *Continental Shelf Research*, *10*(9), 885-894. doi: https://doi.org/10.1016/0278-4343(90)90065-T

Millot, C., & Crépon, M. (1981). Inertial Oscillations on the Continental Shelf of the Gulf of Lions—Observations and Theory. *Journal of Physical Oceanography*, *11*(5), 639 - 657. doi: 10.1175/1520-0485(1981)011⟨0639:IOOTCS⟩2.0.CO;2

Miropol'sky, Y., & Shishkina, O. (2013). *Dynamics of internal gravity waves in the ocean.* Springer Netherlands.

Naveira-Garabato, A. C., Frajka-Williams, E. E., Spingys, C. P., Legg, S., Polzin, K. L., Forryan, A., ... et al. (2019). Rapid mixing and exchange of deep-ocean waters in an abyssal boundary current. *Proceedings of the National Academy of Sciences*, *116*(27), 13233-13238. doi: 10.1073/pnas.1904087116

Odic, R., Bensoussan, N., Pinazo, C., Taupier-Letage, I., & Rossi, V. (2022). Sporadic wind-driven upwelling/downwelling and associated cooling/warming along northwestern mediterranean coastlines. *Continental Shelf Research*, 104843. doi: 10.1016/j.csr.2022.104843

Pastor-Graells, J., Martins, H., Garcia-Ruiz, A., Martin-Lopez, S., & Gonzalez-Herraez, M. (2016). Single-shot distributed temperature and strain tracking using direct detection phase-sensitive otdr with chirped pulses. *Optics express*, *24*(12), 13121–13133. doi: 10.1364/OE.24.013121

Pedregosa, F., Varoquaux, G., Gramfort, A., Michel, V., Thirion, B., Grisel, O., ... et al. (2011). Scikit-learn: Machine learning in Python. *Journal of Machine Learning Research*, *12*, 2825–2830. doi: 10.5555/1953048.2078195

Petrenko, A. (2003). Variability of circulation features in the gulf of lion nw mediterranean sea. importance of inertial currents. *Oceanologica Acta*, *26*, 323–338. doi: 10.1016/S0399-1784(03)00038-0

Quinn, A. J., Lopes-dos Santos, V., Dupret, D., Nobre, A. C., & Woolrich, M. W. (2021). EMD: Empirical Mode Decomposition and Hilbert-Huang Spectral Analyses in Python. *Journal of Open Source Software*, *6*(59), 2977. doi: 10.21105/joss.02977

Reid, E. C., DeCarlo, T. M., Cohen, A. L., Wong, G. T. F., Lentz, S. J., Safaie, A., ... et al. (2019). Internal waves influence the thermal and nutrient environment on a shallow coral reef. *Limnology and Oceanography*, *64*(5), 1949-1965. doi: 10.1002/lno.11162

Rivet, D., de Cacqueray, B., Sladen, A., Roques, A., & Calbris, G. (2021). Preliminary assessment of ship detection and trajectory evaluation using Distributed Acoustic Sensing on an optical fiber telecom cable. *The Journal of the Acoustical Society of America*, *149*(4), 2615-2627. doi: 10.1121/10.0004129

Ruan, X., Thompson, A., Flexas, M., & Sprintall, J. (2017). Contribution of topographically-generated submesoscale turbulence to southern ocean overturning. *Nature Geoscience*, *10*. doi: 10.1038/ngeo3053

Santos, J., & Farahi, F. (Eds.). (2014). *Handbook of Optical Sensors (1st ed.).* CRC Press. doi: https://doi.org/10.1201/b17641

Sartoretto, S., Pairaud, I., Ravel, C. d. V. B., & Chavanon, F. (2022). *Temperature data from the thermistor chain of Cap Vieux (Toulon), North-Western Mediterranean, 2014-2021 time series. SEANOE. [Dataset].* (`https://doi.org/10.17882/86522`)

Seity, Y., Brousseau, P., Malardel, S., Hello, G., Bénard, P., Bouttier, F., ... et al. (2011). The AROME-France Convective-Scale Operational Model. *Monthly Weather Review*, *139*(3), 976 - 991. doi: 10.1175/2010MWR3425.1

Serebryany, A., Khimchenko, E., Popov, O., Denisov, D., & Kenigsberger, G. (2020). Internal waves study on a narrow steep shelf of the black sea using the spatial antenna of line temperature sensors. *Journal of Marine Science and Engineering*, *8*(11). doi: 10.3390/jmse8110833

Shang, Y., Sun, M., Wang, C., Yang, J., Du, Y., Yi, J., ... et al. (2022). Research Progress in Distributed Acoustic Sensing Techniques. *Sensors*, *22*, 6060. doi: 10.3390/s22166060

SHOM. (2015). *MNT Bathymétrique de façade Golfe du Lion – Côte d'Azur (Projet Homonim). [dataset].* (http://dx.doi.org/10.17183/MNT_MED100m_GDL_CA_HOMONIM_WGS84)

Sinnett, G., Davis, K. A., Lucas, A. J., Giddings, S. N., Reid, E., Harvey, M. E., & Stokes, I. (2020). Distributed Temperature Sensing for Oceanographic Applications. *Journal of Atmospheric and Oceanic Technology*, *37*(11), 1987 - 1997. doi: 10.1175/JTECH-D-20-0066.1

Sladen, A., Rivet, D., Ampuero, J. P., Barros, L., Hello, Y., Calbris, G., & Lamare, P. (2019). Distributed sensing of earthquakes and ocean-solid earth interactions on seafloor telecom cables. *Nature Communications*, *10*, 5777. doi: 10.1038/s41467-019-13793-z

Song, H., Chen, J., Pinheiro, L. M., Ruddick, B., Fan, W., Gong, Y., & Zhang, K. (2021). Progress and prospects of seismic oceanography. *Deep Sea Research Part I: Oceanographic Research Papers*, *177*, 103631. doi: 10.1016/j.dsr.2021.103631

Stallone, A., Cicone, A., & Materassi, M. (2020). New insights and best practices for the successful use of empirical mode decomposition, iterative filtering and derived algorithms. *Sci Rep*, *10*(15161). doi: 10.1038/s41598-020-72193-2

Tintoré, J., Wang, D.-P., Garćia, E., & Viúdez, A. (1995). Near-inertial motions in the coastal ocean. *Journal of Marine Systems*, *6*(4), 301-312. doi: 10.1016/0924-7963(94)00030-F

Todd, R. E., Chavez, F. P., Clayton, S., Cravatte, S., Goes, M., Graco, M., ... et al. (2019). Global perspectives on observing ocean boundary current systems. *Frontiers in Marine Science*, *6*. doi: 10.3389/fmars.2019.00423

Traer, T., Gerstoft, P., Bromirski, P., & Shearer, P. (2012). Microseisms and hum from ocean surface gravity waves. *J. Geophys. Res.: Solid Earth*, *117*, B11307. doi: 10.1029/2012JB009550

Trowbridge, J. H., & Lentz, S. J. (2018). The bottom boundary layer. *Annual Review of Marine Science*, *10*(1), 397-420. doi: 10.1146/annurev-marine-121916-063351

Ugalde, A., Becerril, C., Villaseñor, A., Ranero, C. R., Fernández-Ruiz, M. R., Martin-Lopez, S., ... et al. (2021). Noise Levels and Signals Observed on Submarine Fibers in the Canary Islands Using DAS. *Seismological Research Letters*, *93*(1), 351-363. doi: 10.1785/0220210049

van Haren, H., & Millot, C. (2004). Rectilinear and circular inertial motions in the western mediterranean sea. *Deep Sea Research Part I: Oceanographic Research Papers*, *51*(11), 1441-1455. doi: 10.1016/j.dsr.2004.07.009

Van Haren, H., & the ANTARES collaboration. (2014). High-frequency internal wave motions at the antares site in the deep western mediterranean. *Ocean Dynamics*, *64*(4), 507–517.

Vidal-Moreno, P. J., Rochat, E., Fermoso, P., Fernández-Ruiz, M. R., Martins, H., Martin-Lopez, S., ... et al. (2022). Cancellation of reference update-induced 1/f noise in a chirped-pulse DAS. *Optics Letters*, *47*(14), 3588–3591. doi: 10.1364/OL.465367

Villamaña, M., Mouriño-Carballido, B., Marañón, E., Cermeño, P., Chouciño, P., da Silva, J. C. B., ... et al. (2017). Role of internal waves on mixing, nutrient supply and phytoplankton community structure during spring and neap tides in the upwelling ecosystem of ría de vigo (nw iberian peninsula). *Limnology and Oceanography*, *62*(3), 1014-1030. doi: https://doi.org/10.1002/lno.10482

Wang, T., Yang, T., & Xu, W. (2020). Detection and parameter estimation of solitary internal waves using distributed acoustic sensors. *IEEE Access*, *8*, 124223-124235. doi: 10.1109/ACCESS.2020.3006062

Wijffels, S., Roemmich, D., Monselesan, D., Church, J., & Gilson, J. (2016). Ocean temperatures chronicle the ongoing warming of earth. *Nature Climate Change*, *6*. doi: 10.1038/nclimate2924

Williams, E. F., Fernández-Ruiz, M. R., Magalhaes, R., Vanthillo, R., Zhan, Z., González-Herráez, M., & Martins, H. (2019). Distributed sensing of microseisms and teleseisms with submarine dark fibers. *Nature Communications*, *10*. doi: 10.1038/s41467-019-13262-7

Williams, E. F., Zhan, Z., Martins, H. F., Fernández-Ruiz, M. R., Martín-López, S., González-Herráez, M., & Callies, J. (2022). Surface Gravity Wave Interferometry and Ocean Current Monitoring With Ocean-Bottom DAS. *Journal of Geophysical Research: Oceans*, *127*(5), e2021JC018375. doi: 10.1029/2021JC018375

Woodson, C. (2018). The fate and impact of internal waves in nearshore ecosystems. *Annual review of marine science*, *10*(1). doi: 10.1146/annurev-marine-121916-063619

Wu, W., Zhan, Z., Peng, S., Ni, S., & Callies, J. (2020). Seismic ocean thermometry. *Science*, *369*(6510), 1510–1515. doi: 10.1126/science.abb9519

Zhu, X.-W., Zhang, S.-J., & Liu, Q.-L. (2015). Determination to the Confidence Level of PSD Estimation with Given D.O.F. Based on WELCH Algorithm. In *Proceedings of the 4th international conference on information technology and management innovation* (p. 617-622). doi: 10.2991/icitmi-15.2015.101

Supporting Information for "High resolution seafloor thermometry and internal wave monitoring using Distributed Acoustic Sensing"

Julián Pelaez Quiñones[1], Anthony Sladen[1], Aurelien Ponte[2], Itzhak Lior[3],

Jean-Paul Ampuero[1], Diane Rivet[1], Samuel Meulé[4], Frédéric Bouchette[4],

Ivane Pairaud[2], Paschal Coyle[5]

[1]Université Côte d'Azur, CNRS, Observatoire de la Côte d'Azur, IRD, Géoazur, Sophia Antipolis, *250* rue Albert Einstein, *06560*, Valbonne, France

[2]IFREMER, Université de Brest, CNRS, IRD, Laboratoire d'Océanographie Physique et Spatiale, IUEM, Brest, France

[3]Institute of Earth Sciences, The Hebrew University, Jerusalem, Israel

[4]Geosciences-M/GLADYS, Université de Montpellier, CNRS, Montpellier, France

[5]Aix-Marseille Université, CNRS/IN2P3, CPPM, Marseille, France

Contents of this file

1. Text S1 to S5
2. Figures S1 to S2

Introduction

This file contains complementary information to our main manuscript, principally details about the sensing instruments, methods, processing and some additional figures.

Text S1. Principle of Distributed Acoustic Sensing

Distributed Acoustic Sensing (DAS) systems make use of single optic fibers cased inside (un)armored cables, for instance existing Telecommunication cables, to sense the environment. So far, DAS systems require a dark fiber to operate. Coherent laser pulses are regularly sent along the fiber and their Rayleigh back-scattered signature is used as a proxy for temperature and strain perturbations affecting the optical path length (due to local elongations and refractive index variations of the fiber) over specific sections of the cable, which can be localized (López-Higuera, 2002; Hartog, 2017). These perturbations are traced-back along the fiber by converting the two-way travel time of light to distances with the known speed of light in silica. Measurements are averaged along a few meters of cable (gauge length) at a defined distance step (spatial sampling). In contrast to DAS, Distributed Temperature Sensing (DTS) is based on Raman-scattering, while Distributed Temperature and Strain Sensing (DSTS) is based on Brillouin-scattering.

The DAS interrogator unit used for our main analysis is an ϕ-OTDR hDAS (High fidelity distributed acoustic sensor) designed by Aragón Photonics, which provides measurements in strain units. One specificity of the hDAS system is the fact that it sends a chirped light signal. Details can be found in (Pastor-Graells et al., 2016; Fernández-Ruiz et al., 2019). The sampling frequency was 100 Hz in the first couple days of the campaign and then switched to 500 Hz.

The DSTS system used to validate the simultaneous LF-DAS (indirect) measurements was a Febus Optics G1-C set to record with a gauge length of 10 m and sampling resolution of 2.0 m over 30 km. The temporal sampling was set to 15 min to keep the data noise level at a reasonable level. The DAS system in this case was a Febus A1-R DAS interrogator with gauge length of 10 m and sampling resolution of 4.8 m over 40 km of cable.

Text S2. Extracting the low-frequency component of DAS data

Because of the high sampling rates and large DAS data volumes acquired, a conventional low-pass filtering approach was not possible to isolate the low-frequency content of the raw data. Thus, a parallel-computing approach with a moving average was instead implemented for efficiency in the reduction of the thousands of channels

We implemented a moving average windows of 5 minutes with 60% overlap independently to each channel. This implies an output sampling frequency of ∼8.33 mHz and a maximum resolvable frequency of ∼1.66 mHz (the latter is the inverse of twice the averaging window and does not necessarily match the Nyquist-criterion frequency that would be expected from the data point sampling rate). Our experience with different windows showed this combination to be a good compromise between a smoothing that is not excessive as to preserve the LF content, while being enough to remove spikes, high frequency noise, and to reduce the data size by a considerable proportion

The original data acquired is automatically segmented in sections of several days due to a laser refreshing procedure of the interrogator. Each segment has different trends, large value offsets and most of the times gaps in between. We demean the first segment and adjust the remaining segments with respect to the last value of the previous ones to ensure continuity between them and to smooth-out large data breaks. This is performed for each channel separately. Although some of the consecutive segments show different trends which are likely related to instrumental drift, we did not correct these to avoid distorting and losing true signal, since an objective instrumental drift correction function is unknown to us. The data gaps in the signal were filled using cubic interpolation between segments. This allows for processing routines that require continuous time series (spectral decomposition and filtering). In this exploratory stage, we do not filter out "bad quality" channels, given that a criteria to define their "usefulness" (which may or may not be related to ground-seabed coupling) is not yet completely understood. A last pre-processing step is to remove the along channel mean amplitude temporal fluctuation from each sample of the data (DAS temporal response or common-noise correction) using a band of channels around a central channel to find each average. This procedure provides smoother time series, while the effect of the laser time fluctuations and strong amplitude spikes/steps is minimized. The data was highpass-filtered at 0.009 mHz prior to frequency-wavenumber transformation using a 2D Direct Fourier Transform.

Text S3. Conversion of strain to temperature

As outlined in Ide, Araki, and Matsumoto (2021), at long time scales (low frequencies), the apparent strain differences are expected to be caused by refractive index variations of the fiber due to temperature changes in the environment, instead of being caused by LF strain-related elongations on the fiber, since such LF strains could hardly couple energy into the fiber and their effect is much smaller in magnitude than the temperature effect. The formula that approximately describes this variations is:

$$\frac{\mathrm{d}\epsilon}{\mathrm{d}T} = n\alpha + \frac{\mathrm{d}n}{\mathrm{d}T}$$

where ϵ, T, n and α represent the observed (apparent) strain, the environment's temperature, silica's refractive index (typically around $7 \cdot 10^{-6}$ K^{-1} at room temperature) and its thermal expansion coefficient, respectively. The authors explain that a typical value for $\mathrm{d}n/\mathrm{d}T$ is 10^{-5} (constant) while the $n\alpha$ term is expected to be much smaller, in the order of 10^{-7}. Under these assumptions, a $\Delta s = 1$ nanostrain difference is approximately equivalent to $\Delta T = 0.1$ mK.

An absolute difference-normalization of each separate LF-DAS channel, i.e. between zero and the maximum value of each channel, is applied before conversion to temperature differences.

For the comparison of LF-DAS with the thermistor chain in Fig. 2, the best-matching cable channel was found via cross-correlation maxima search. The maximum correlations were found with the deepest, 50 m deep, temperature sensor of Cap Vieux, which is almost touching the seafloor and better replicates the FO cable configuration. We note, however, that the maximum normalized correlations have spread maxima at roughly 60%, i.e. the highest correlations near zero-lag were similar over a range of a few tens of channels; this result is expected given that both sensors are not collocated but separated by a few kilometers. The best-matching LF-DAS channel is located ∼4 km away from the thermistor chain.

As outlined in the main text, the FO inside the Toulon cable is relatively loose and can creep inside the cable when deformed slowly, at very low-frequencies. When rapidly deformed by e.g. high-frequency seismic or acoustic waves, it responds proportionally to the stresses without creeping. This further contributes to explain why at LF, the effect of temperature is dominant whereas strains appears negligible.

Text S4. Inertial variability

The inertial period T_c at a given latitude θ reflects the variability time scale of important mesoscale to large scale oceanographic processes. This period is determined by the Coriolis effect due to the angular momentum conservation for traveling objects that are subjected to the earth's rotation centrifugal force and can be estimated via:

$\mathrm{T}_c = {f_c}^{-1} = (2\Omega \sin\theta)^{-1}$

where f_c is known as the Coriolis frequency and Ω is the rotation rate of the earth ($\sim 7.29 \times 10^{-5}$ rad/s). This translates into an inertial period of ∼17.5h at the mean latitude of the Toulon cable (43°N).

Text S5. Empirical Mode Decomposition and Hilbert-Huang Transform Parameters

EMD and HHT analyses (Huang et al., 1998) were performed by using the EMD Python package developed by Quinn, Lopes-dos Santos, Dupret, Nobre, and Woolrich (2021). Several of the examples and built-in functions of the package were implemented in our study. The mask sifting (mode separation) scheme (Deering & Kaiser, 2005) produced the best results for the LF-DAS data. This approach allows us to obtain a set of well-behaved Intrinsic Mode Functions (IMFs) that represent generalized spectral components or empirical modes of the input signal. A proper sifting leads to IMFs that are purely oscillatory functions with zero reference levels from which instantaneous amplitude and frequency attributes are obtained by means of a Hilbert-Huang Transform (HHT) (Huang & Wu, 2008). The masks are monochromatic signals introduced into the Intrinsic Mode Function (IMF) under consideration to avoid mixing of modes with very different frequencies: as the high frequency components are always captured and separated first during the sifting, a mask signal with a frequency higher than a long period oscillation in the signal contributes to separate the latter correctly from the other higher frequency components. Most of the default mask sifting parameters of the package were the basis of our processing. The amplitude of these masks were uniformly computed as ratios of the standard deviation of the input for all IMFs; their frequency successively increasing at factors of 2. Four masks were applied to each IMF and the sift threshold was set to 10^{-8}. Eight IMFs were calculated in total.

The instantaneous attributes (amplitude and frequency) of each IMF were found via amplitude-normalized Hilbert transform (NHT) as in (Huang et al., 2009). Channels with anomalous extrema were muted under a 3-standard deviation outlier criterium. We applied a logarithmic binning of 1000 grid points between 0.001 and 1.0 mHz to ensure enough spectral resolution. Amplitudes were stacked to obtain the binned HHT. The HHT spectra were normalized as power spectral density (divided by $f_{sampling} \cdot N_{samples}$). To obtain the HHT spectra, we averaged all the instantaneous attributes of each IMF over a selected range of channels. This results in a stacked spectrogram-like output representing the dominant spectral power spectral density over a section of cable. The LF-DAS time series were pre-filtered with a highpass at 0.0007 mHz (equivalent to nearly 16 days - the total duration of the deployment) and pre-averaged every two consecutive channels to increase their SNR. The final images were smoothed using a Gaussian kernel convolution filter with one standard deviation. For Figs 3b,c, each IMF is weighted by its instantaneous amplitude, so to obtain an image analogous to a spectrogram that captures the time-evolution of the spectral components.

Care was taken to select a timespan for analysis with no large data breaks and to reject channels with anomalously uniform or large values or spikes (as seen from Fig. 2a,b), as these artifacts can largely affect the EMD (Stallone et al., 2020). Furthermore, the averaging of the instantaneous attributes of each IMFs across a sufficiently long cable range helps to balance out such undesired effects, in case that artifacts may remain at some channels. Supplementary Figure S1 shows an example of such decomposition for a selected channel using the EMD Python package.

References

Deering, R., & Kaiser, J. (2005). The use of a masking signal to improve empirical mode decomposition. In *Proceedings. (icassp '05). ieee international conference on acoustics, speech, and signal processing, 2005.* (Vol. 4, p. iv/485-iv/488 Vol. 4). doi: 10.1109/ICASSP.2005.1416051

Fernández-Ruiz, M. R., Costa, L., & Martins, H. F. (2019). Distributed acoustic sensing using chirped-pulse phase-sensitive otdr technology. *Sensors*, *19*(20), 4368. doi: 10.3390/s19204368

Hartog, A. (2017). *An Introduction to Distributed Optical Fibre Sensors* (1st ed.). CRC Press. doi: 10.1201/9781315119014

Huang, N. E., Shen, Z., Long, S. R., Wu, M. C., Shih, H. H., Zheng, Q., ... et al.

(1998). The empirical mode decomposition and the Hilbert spectrum for nonlinear and non-stationary time series analysis. *Proc. R. Soc. Lond. A.*, *454*, 903–995. doi: 10.1038/s41598-020-72193-2

Huang, N. E., & Wu, Z. (2008). A review on Hilbert-Huang transform: Method and its applications to geophysical studies. *Reviews of Geophysics*, *46*(2). doi: 10.1029/2007RG000228

Huang, N. E., Wu, Z., Long, S. R., Arnold, K. C., Chen, X., & Blank, K. (2009). On instantaneous frequency. *Advances in Adaptive Data Analysis*, *01*(02), 177-229. doi: 10.1142/S1793536909000096

Ide, S., Araki, E., & Matsumoto, H. (2021). Very broadband strain-rate measurements along a submarine fiber-optic cable off cape muroto, nankai subduction zone, japan. *Earth Planets Space*, *73*(63). doi: 10.1186/s40623-021-01385-5

López-Higuera, J. M. (Ed.). (2002). *Handbook of Optical Fibre Sensing Technology* (1st ed.). John Wiley & Sons, ltd.

Pastor-Graells, J., Martins, H., Garcia-Ruiz, A., Martin-Lopez, S., & Gonzalez-Herraez, M. (2016). Single-shot distributed temperature and strain tracking using direct detection phase-sensitive otdr with chirped pulses. *Optics express*, *24*(12), 13121–13133. doi: 10.1364/OE.24.013121

Quinn, A. J., Lopes-dos Santos, V., Dupret, D., Nobre, A. C., & Woolrich, M. W. (2021). EMD: Empirical Mode Decomposition and Hilbert-Huang Spectral Analyses in Python. *Journal of Open Source Software*, *6*(59), 2977. doi: 10.21105/joss.02977

Stallone, A., Cicone, A., & Materassi, M. (2020). New insights and best practices for the successful use of empirical mode decomposition, iterative filtering and derived algorithms. *Sci Rep*, *10*(15161). doi: 10.1038/s41598-020-72193-2

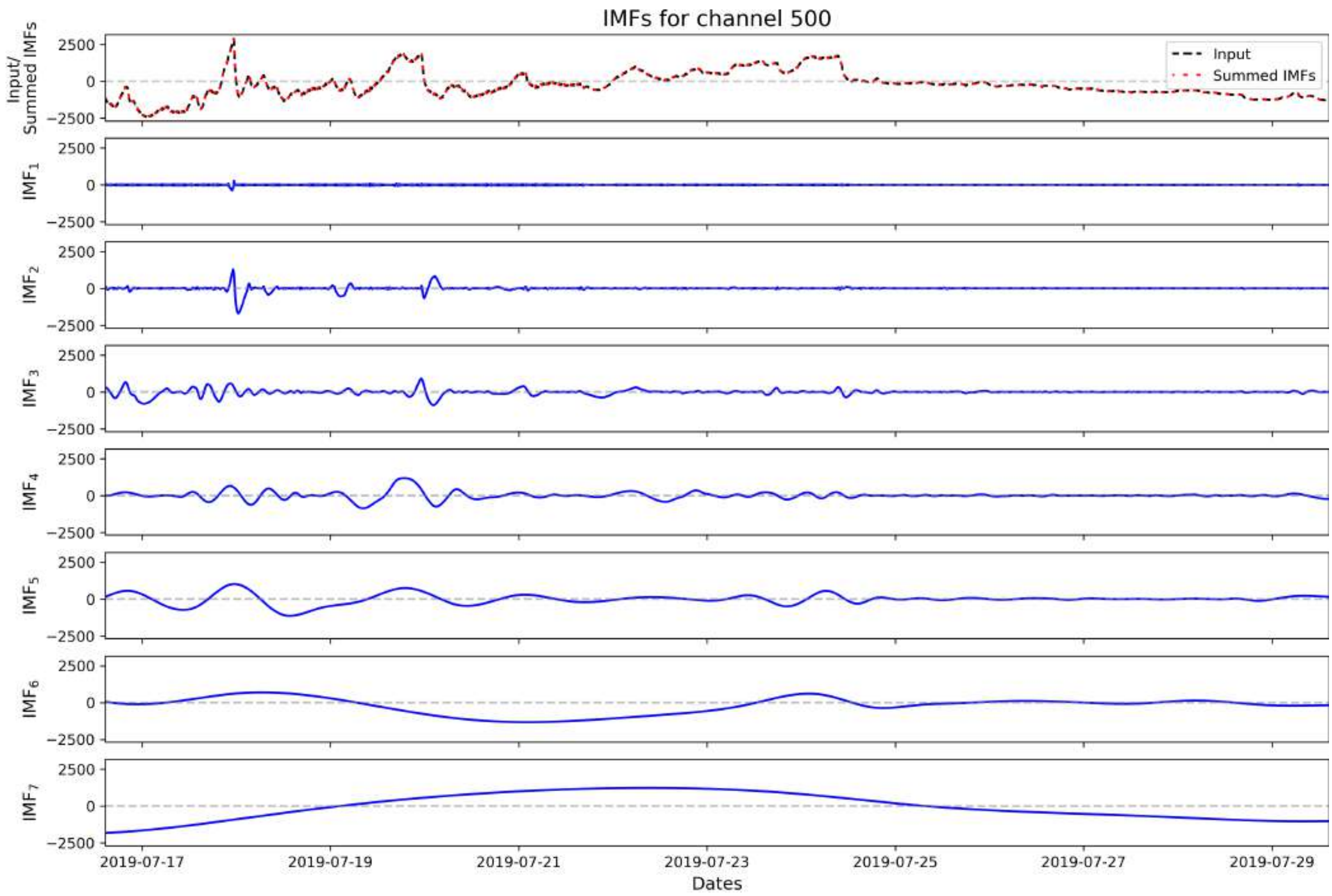

Figure S1. Sample Intrinsic Mode Functions (IMFs) for a selected LF-DAS channel.

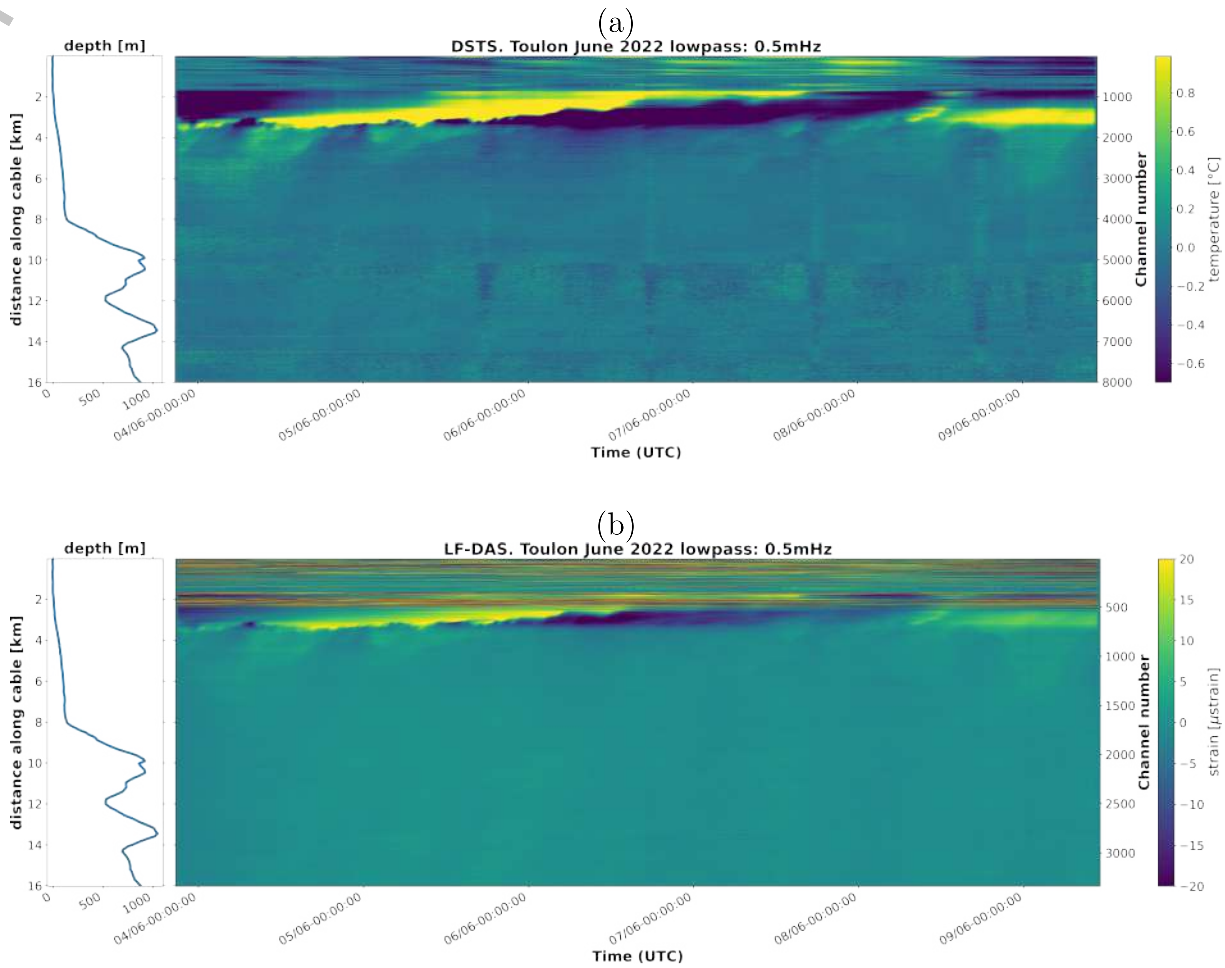

Figure S2. Collocated DSTS and LF-DAS measurements in Toulon, June 2022 - Filtered ensemble comparison. Lowpassed DSTS (a) and LF-DAS (b)

(c)

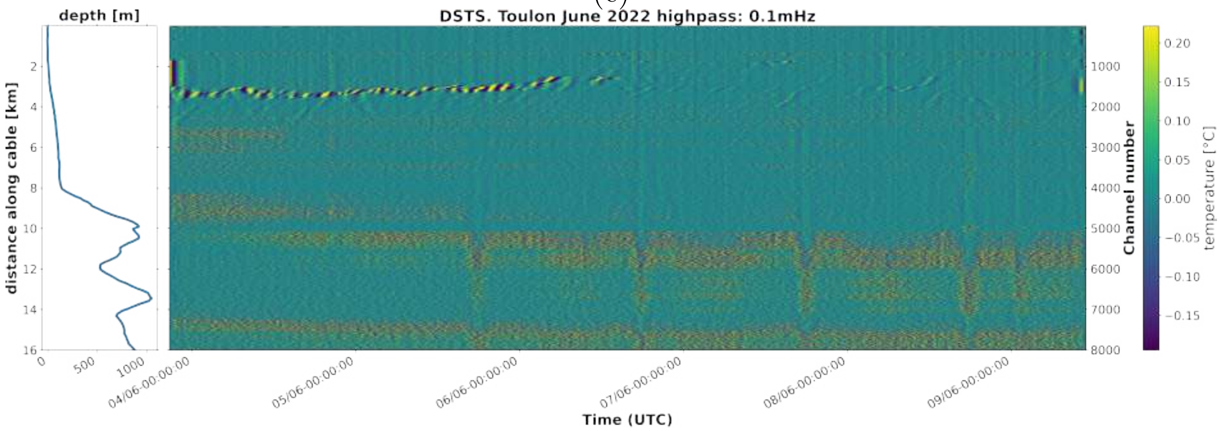

(d)

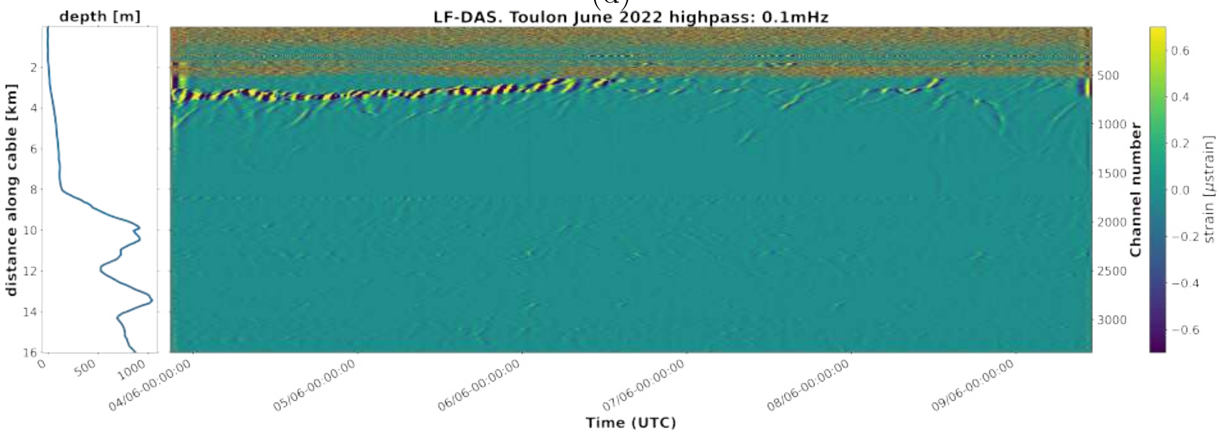

Figure S2. (cont.) collocated DSTS and LF-DAS measurements in Toulon, June 2022 - Filtered ensemble comparison. Highpassed DSTS (c) and LF-DAS (d).